AIAA SciTech Forum
8–12 January 2018, Kissimmee, Florida
2018 AIAA Aerospace Sciences Meeting

10.2514/6.2018-2200

Effect of Different Operational Parameters on the Rarefied Gas Electro Jet (RGEJ) Performance

Ariel Blanco[1] and Subrata Roy[2]
Applied Physics Research Group
University of Florida, Gainesville, FL, 32603, USA

This article numerically investigates a micro-thruster for small satellites that utilizes plasma actuators to heat and accelerate the flow in a microchannel with rarefied gas in the slip flow regime. The inlet plenum condition is considered at 1.0 *Torr* with flow discharging to a near vacuum condition (~ 0.05 *Torr*). The Knudsen numbers at the inlet and exit planes are ~ 0.01 and ~ 0.1, respectively. Numerical simulations of the charge distribution due to gas ionization processes and the resulting rarefied gas flow are performed using an in-house code. The mass flow rate, thrust, specific impulse, and power consumption of the thruster are predicted based on these results. The ionized gas is modeled using local mean energy approximation. An electrically induced body force and a thermal heating source are calculated based on the space separated charge distribution and the ion Joule heating, respectively. The rarefied gas flow, with these electric force and heating source, is modeled using density-based compressible flow equations with slip flow boundary conditions and ideal gas assumption. Previously, an integrated study of the glow discharge physics and resulting fluid flow of the plasma thruster under these low pressure and low Knudsen number conditions was published by our group (J. Phys. D, 455201, 2017). The previous results show that a significant improvement of specific impulse can be achieved over highly optimized cold gas thrusters using the same propellant. In this paper, we examined the effect of using a higher tangential accommodation coefficient and found that it produces higher specific impulse, thrust effectiveness, and total efficiency.

I. Nomenclature

ρ	=	density
u, v	=	*x and y* components of velocity
T	=	temperature
P	=	pressure
F_x, F_y	=	*x and y* components of the volumetric plasma-induced electrostatic force
q'''	=	volumetric plasma-induced electrothermal heating source
V	=	voltage
I	=	current
P_W	=	power
Kn	=	Knudsen number
k_B	=	Boltzmann constant
Re	=	Reynolds number
μ	=	absolute viscosity
κ	=	thermal conductivity
R	=	gas constant
$\dot{m}$	=	mass flow rate
F_{Thrust}	=	thrust
$F_{\tau_{Wall}}$	=	shear force
I_{sp}	=	specific impulse
ζ_{Thrust}	=	thrust effectiveness
η_T	=	total efficiency

[1] Graduate Student, Mechanical and Aerospace Engineering, blanco07@ufl.edu, AIAA Student Member.
[2] Professor, Mechanical and Aerospace Engineering, roy@ufl.edu, AIAA Associate Fellow.

II. Introduction

SMALL satellites have gained interest in recent years due to their smaller overall life cycle cost as well as their short delivery time from concept to launch (2-3 years) [1]. However, the miniaturization of their propulsion system faces several technical challenges such as contamination, passage clogging, less reliability, less durability, and excessive complexity. Micro-thrusters must produce minimum impulse bits of $\mathcal{O}(\mu N \cdot s)$ determined by attitude control requirements [1]. In contrast, the thrust requirement for slew maneuvers extends into the $\mathcal{O}(mN)$ range, very large when compared to the impulse bits requirements. Micro-propulsion systems must overcome these problems while being lightweight, compact, low power, efficient, and inexpensive.

A cold gas thruster (CGT) is the simplest case of a thermal rocket, in which the heat capacity of the gas serves as the thermal source. CGTs have desirable advantages for micro-propulsion applications such as low system complexity, reliability, small impulse bit capabilities, and no contamination problems when benign propellant is used (e.g., N_2) [1]. The Moog 58×125, an example of a micro-CGT, has small minimum impulse bits of 100 $\mu N \cdot s$, a relatively large thrust of 4.5 mN, and a specific impulse of 64 s when nitrogen at a plenum pressure of 34.5 kPa is used as the propellant [1]. However, valve leakage for low molecular mass propellants or low specific impulse (I_{sp}) for desirable propellants, eliminate CGT from consideration for primary propulsion tasks unless the required $\Delta - \mathrm{v}$ is small (< 100 *m/s*) [1]. Their I_{sp} is typically low unless very light gases are used (e.g., H_2 or He), which produce experimentally measurable specific impulses of 272 and 165 s, respectively [1]. Very light gases are commonly not used due to storage problems (valve leakage and heavier tanks). For argon propellant, the I_{sp} of a highly optimized cold gas thruster is 52 s [1]. In the simplest approximation, the I_{sp} of a CGT is proportional to the square root of the gas temperature. In a resitojet, the performance of the thruster is increased by heating the gas using an electrical resistance.

In order to increase the I_{sp} of CGT, the free molecule micro-resistojet (FMMR) was proposed [1]. FMMR operates at low stagnation pressures (50 - 500 Pa) and large exit Knudsen numbers ($Kn \sim 1$) [1]. Due to the low pressures, gas heating occurs primarily by conduction [2]. FMMR operating with a heating element temperature of 600 K can produce an I_{sp} of 68 s for water and 45 s for argon propellant [1]. These values may not look as an improvement, but due to the low stagnation pressure, liquid propellant could be stored at its vapor pressure and vaporized on demand, thus avoiding heavy storage tanks and valve leakage [1]. An estimated by Ketsdever, Wadsworth, and Muntz [3] predicts that for a N_2 -propellant CGT with a tank pressure of 20 *MPa* and a temperature of 300 *K,* the ratio of tank mass to propellant mass is approximately 0.483 if graphite is used (or 1.0 if titanium), decreasing the effective I_{sp} of the device by 30 – 50%. Due to the low plenum pressure of FMMR, the tank mass is expected to be negligible if H_2O is used as the propellant. Unfortunately, FMMR suffers from significant thermal energy losses due to thermal dissipation [4]. An estimate by Micci and Ketsdever [1] predicts a heat loss of 6800 mW for a device operating with 40 expansion slots that requires 6000 to 8000 mW to heat the propellant gas [1].

The proposed rarefied gas electro jet (RGEJ [5]) micro-thruster aims to decrease the heat loss of microelectromechanical (MEMS) based microresistojet thruster designs by increasing the efficiency of the energy exchange from the electrical source to the propellant [6]. It operates in the slip flow regime, which decreases viscous losses and heat transfer to the walls. The RGEJ concept involves localized embedding of electrodes with either a DC or an RF applied potential difference, along the dielectric walls to produce a glow discharge plasma [4]. The charged particles in the plasma are accelerated by the electric field, heating the propellant. The presence of charged particles implies that both electric and magnetic fields could be used to produce thrust. In this study, magnetic fields are not used and the thruster operates with a DC obstructed glow discharge. A finite element and a finite difference based numerical analysis of the rarefied gas and the ionized gas are implemented, respectively, to model the RGEJ. The cases presented, display a non-optimized design with adiabatic walls and a low plenum pressure (1.0 *Torr*), operating at 750 *V*. It is important to emphasize that adiabatic walls, instead of isothermal, requires a more robust iterative procedure between the loosely coupled code modules.

III. Methodology

In order to simulate the RGEJ, an existing, previously described in literature, in-house modular Multi-scale Ionized Gas (MIG) flow solver platform developed by Roy *et al.* [7, 8] was used. The MIG code consists of two modules: a finite element based *rarefied gas module* (RGM) and a finite difference based *ionized gas module* (IGM), which was recently developed. They are loosely coupled in the following sequence. The RGM runs until convergence, producing the gas density (ρ), components of velocity (u, v), and temperature (T). These variables from the RGM are passed to the IGM. Then, the IGM runs until convergence, producing the volumetric plasma-induced electrostatic force components (F_x, F_y) and the volumetric plasma-induced electrothermal heating source (q''') needed by the new run of the RGM. The information obtained by each module is exchanged in this fashion until the steady-state solution is obtained. In Fig. 1, this process is shown.

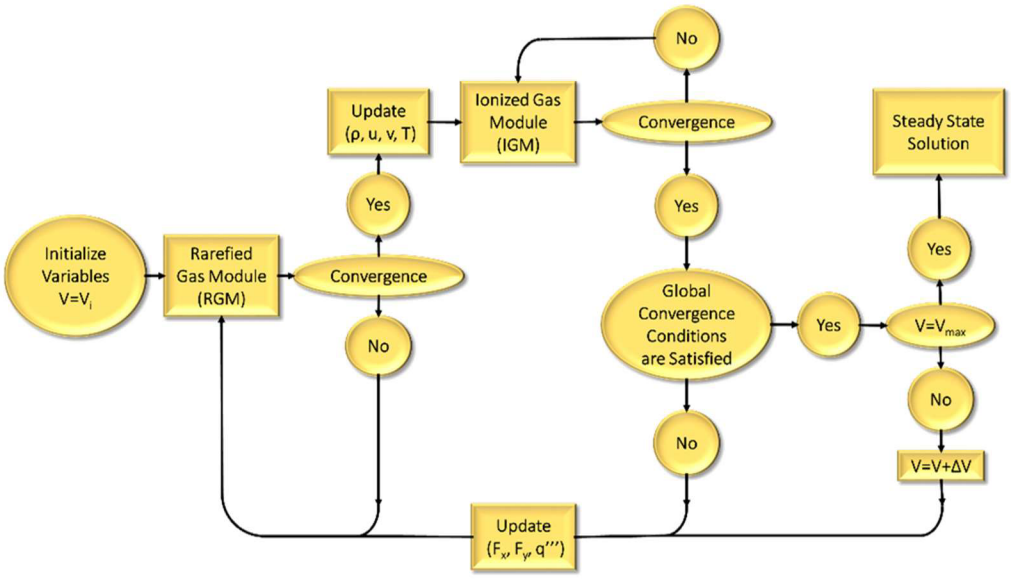

Fig. 1 Schematic of the new MIG code with rarefied gas and ionized gas modules.

The first step in the program initializes the variables of both modules, including the initial voltage (V_i = 150 V) value, based on the plasma breakdown voltage of the gas. Each module uses the L^2-norm of the solution to test for convergence. After both modules have reached convergence at a given voltage, the voltage is increased by a voltage difference (ΔV) and the process is repeated, until the maximum voltage (V_{max}) desired is achieved. For all cases in this study, (ΔV) is 50V. The L^2-norms for the RGM and the IGM, using the given non-dimensionalization explained in the following sections, are 10^{-4} and 10^{-10} for time steps of 10^{-8} and 5×10^{-13} seconds for each module, respectively.

IV. Ionized Gas Module (IGM)

The numerical model for the argon plasma assumes a weakly ionized gas composed of positive ions, three types of metastable atoms, and electrons. In fluid models of glow discharges, all plasma species are treated as a continuum. Momentum equations are usually reduced to the drift-diffusion equation. In the local mean energy approximation (LMEA) model, the spatial distribution of the electron temperature is obtained from the solution of the energy balance equation for electrons [9]. The calculation of the electron transport coefficients (mobility and diffusion) and the kinetic coefficients (electron-impact reaction rates for excitation and ionization processes) are done by solving the kinetic Boltzmann equation as functions of the electron energy [9].

A. Plasma Governing Equations and Argon Chemistry

The continuity equation that is solved for each plasma species is given in Eq.(1) [10].

$$\frac{\partial n_k}{\partial t} + \nabla \cdot \Gamma_k = S_k$$
$$\Gamma_k = \mathrm{sgn}(q_k)\mu_k n_k \boldsymbol{E} - D_k \nabla n_k + n_k \boldsymbol{V} \tag{1}$$

The right-hand-side (RHS) of Eq. (1) contains the source and sink terms representing the argon chemistry, similar in notation to Rafatov, Bogdanov, and Kudryavtsev [11]. The subscript k is equal to: i, e, S, P, or D, for ions, electrons, and three types of metastable atoms, respectively. $\boldsymbol{V}$ is the velocity vector of the bulk gas obtained from the *rarefied gas module* [12]. The electron energy equation is included in LMEA in order to incorporate the nonlocal transport of electrons written as recommended by Hagelaar and Pitchford [13].

$$\frac{\partial n_\varepsilon}{\partial t} + \nabla \cdot \Gamma_\varepsilon = -\mathrm{e}\Gamma_\mathrm{e} \cdot \mathrm{E} - \frac{3}{2} n_\mathrm{e} \frac{2m_\mathrm{e}}{m_n} \nu_{\mathrm{en}} k_\mathrm{B} \left(T_\mathrm{e} - T_{gas}\right) - \mathrm{e} \sum_l \Delta E_l^\mathrm{e} r_l$$
$$\Gamma_\varepsilon = -\mu_\varepsilon n_\varepsilon \boldsymbol{E} - D_\varepsilon \nabla n_\varepsilon + \frac{5}{3} n_\varepsilon \boldsymbol{V} \tag{2}$$

The first term on the RHS of Eq. (2) describes the Joule heating, which is responsible for adding energy to electrons. The second and third term describe the electron energy losses due to the inelastic and elastic collisional processes [14], where ν_{en} is the electron atomic elastic collision, ΔE_l^e is the energy loss (or gain) due to inelastic collisions during the reaction r_l (e.g., $r_2 = R_2 n_n n_e$) and m is the mass of the given particle. The elementary reactions considered for low-pressure, argon chemistry are given in table 1 in Blanco and Roy [6].

The electron transport coefficients μ_e and D_e are calculated using an electron Boltzmann equation solver, BOLSIG+ [13], as functions of the mean electron energy [$\varepsilon = (3/2)k_B T_e$] and the energy transport coefficients are related to the particle transport coefficients via $\mu_\varepsilon = (5/3)\mu_e$ and $D_\varepsilon = (5/3)D_e$. The ion mobility and diffusion coefficients are obtained from Rafatov, Akbar, and Bilikmen [15], and the Einstein relation ($D_i = k_B T_i \mu_i / e$), respectively, where the electric field ($\boldsymbol{E}$) is in *V/m* and the neutral number density (n_n) is in m^{-3}, giving a mobility in $m^2/(Vs)$.

$$\mu_i = \left(\frac{4.411\times10^{21}}{n_n}\right)\left(1+\left(7.721\times10^{-3}\left(10^{21}\frac{|\boldsymbol{E}|}{n_n}\right)\right)^{3/2}\right)^{-0.33} \tag{3}$$

The metastable mobility is zero for all the metastable species in this model and the metastable diffusion is the same as in Deconinck [16]. All heavy species, metastable and ion species, are assumed to be in thermal equilibrium with the gas. The volume source terms (S_k) in Eq. (1) are determined by the reactions occurring within the discharge, where the source terms (S_i, S_e) for ions and electrons are identical due to particle conservation. The subscript (*rev*) in some of the reaction rates (R_l) is for the reverse reaction.

$$S_e = S_i = R_2 n_n n_e + R_6 n_S n_e + R_7 n_P n_e + R_8 n_D n_e + R_{11} n_S n_S + R_{12} n_P n_P + R_{13} n_S n_P \tag{4}$$

$$S_S = R_3 n_n n_e - R_{3(\mathrm{rev})} n_S n_e - R_6 n_S n_e - R_9 n_S n_e + R_{9(rev)} n_P n_e - 2R_{11} n_S n_S - R_{13} n_P n_S + R_{14} n_P n_n n_n + R_{15} n_P n_n - R_{16} n_S + R_{18} n_P \tag{5}$$

$$S_P = R_4 n_n n_e - R_{4(\mathrm{rev})} n_P n_e - R_7 n_P n_e + R_9 n_S n_e - R_{9(\mathrm{rev})} n_P n_e - 2R_{12} n_P n_P - R_{13} n_P n_S - R_{14} n_P n_n n_n - R_{15} n_P n_n - R_{18} n_P + R_{19} n_D \tag{6}$$

$$S_D = R_5 n_n n_e - R_{5(\mathrm{rev})} n_D n_e - R_8 n_D n_e + R_{10} n_P n_e - R_{10(\mathrm{rev})} n_D n_e - R_{17} n_D - R_{19} n_D \tag{7}$$

The neutral species number density (n_n) is solved using the ideal gas law.

$$P_{gas} = k_B \left(n_n + \underbrace{n_i + n_S + n_P + n_D}_{\ll n_n} \right) T_{gas} + k_B n_e T_e \tag{8}$$

The system of equations is closed with the solution of the electrostatic Poisson equation in order to calculate the electric field, where Z_k is the ionizity (or valence) of the given charged particles and $\in_0$ is the permittivity of free space. Argon relative permittivity is $\in_r \sim 1.0$ [9].

$$\epsilon_0 \nabla \cdot \boldsymbol{E} = \sum_{\mathrm{k}} Z_{\mathrm{k}} e n_{\mathrm{k}}$$
$$\boldsymbol{E} = -\nabla \phi \tag{9}$$

The governing equations are written in the non-dimensional form using reference number density of 10^{16} m^{-3}, an electric potential of 100 V, a length scale of 0.01 m, an electron temperature of 10 eV and a time scale of 10^{-10} s.

B. Plasma Boundary Conditions

The boundary conditions for ions, electrons, metastable atoms, and electron energy density at the anode, cathode, and dielectric surfaces (walls) are the same as in Rafatov, Bogdanov, and Kudryavtsev [9], where the secondary electron emission coefficient (γ_{sec}) is selected to have a value of 0.07 [17].

$$\boldsymbol{\Gamma_e} \cdot \hat{n}_w = \underbrace{\frac{1}{4} n_e v_{th,\mathrm{e}}}_{\text{Thermal flux}} + \underbrace{\alpha_e n_e \mu_e \left(\boldsymbol{E} \cdot \hat{n}_w\right)}_{\substack{\text{Electron drift flux = 0} \\ \text{for obstructed glow} \\ \text{discharges}}} - \underbrace{\sum_i \gamma_{\mathrm{sec}} \left(\boldsymbol{\Gamma_i} \cdot \hat{n}_w\right)}_{\substack{\text{Secondary Electron Emission} \\ (\gamma_{\mathrm{sec}} = 0.07) \text{ only at cathode}}} \tag{10}$$

$$\boldsymbol{\Gamma_i} \cdot \hat{n}_w = \underbrace{\frac{1}{4} n_i v_{th,i}}_{\text{Thermal flux}} + \underbrace{\alpha_i n_i \mu_i \left(\boldsymbol{E} \cdot \hat{n}_w\right)}_{\text{Ion drift flux}} \tag{11}$$

$$\boldsymbol{\Gamma_k} \cdot \hat{n}_w = \underbrace{\frac{1}{4} n_k v_{th,k}}_{\text{Thermal flux}} \quad \text{for } k = S, P, \text{ or } D \tag{12}$$

$$\boldsymbol{\Gamma_\varepsilon} \cdot \hat{n}_w = 2 k_B T_e \left(\boldsymbol{\Gamma_e} \cdot \hat{n}_w\right) \tag{13}$$

In the previous equations, the following parameters are needed to complete them, and $\hat{n}$ is the unit vector normal to the surface.

$$\begin{aligned} &\text{If } \operatorname{sgn}\left(Z_k\right)\left(\boldsymbol{E} \cdot \hat{n}_w\right) > 0 \text{ then } \alpha_k = 1, \text{ else } \alpha_k = 0 \\ &v_{th,k} = \sqrt{8 k_B T_k / \left(\pi m_k\right)} \\ &\varepsilon = \frac{n_\varepsilon}{n_e} = \frac{3}{2} k_B T_e \end{aligned} \tag{14}$$

For the electric potential boundary conditions, (ϕ) is equal to the zero at the anode and to the negative value of the discharge voltage at the cathode, whereas at the dielectric surface, the surface charge equation is used [9].

$$\begin{aligned} \frac{\partial \sigma}{\partial t} &= \sum_k Z_k e \left(\boldsymbol{\Gamma_k} \cdot \hat{n}_w\right) \\ \underbrace{\frac{\partial \phi}{\partial r} = \frac{1}{\epsilon_0} \sigma}_{r = \text{ distance from surface}} & \end{aligned} \tag{15}$$

The charged or metastable species impacting the surface are assumed to recombine instantly at the solid walls.

Symmetry condition is imposed at the bottom of the channel since only half of the domain is simulated. Zero particle flux is imposed for the inlet for numerical stability reasons.

$$\Gamma_{\mathrm{x,\,k}} = 0,\ \Gamma_{\mathrm{x,\,\varepsilon}} = 0,\ \left.\frac{\partial \phi}{\partial x}\right|_{x=0} = 0 \tag{16}$$

The inlet boundary is sufficiently far away from the cathode region and has no influence on the plasma output parameters: $\boldsymbol{F}$ and q''' [16].

In an open face boundary, the particles are assumed to flow out of the domain with the velocity of the bulk gas, flux conditions are imposed for all particles, and homogeneous Neumann condition is used for the electric potential. Open face is imposed for the exit plane.

$$\Gamma_{\mathrm{x,\,k}} = V_x n_k,\ \Gamma_{\mathrm{x,\,\varepsilon}} = \frac{5}{3} V_x n_k,\ \left.\frac{\partial \phi}{\partial x}\right|_{x=L} = 0 \tag{17}$$

where $V_x = u$

C. Volumetric Electrostatic Force and Volumetric Electrothermal Heating Source

The volumetric plasma-induced electrostatic force and volumetric plasma-induced electrothermal heating source are calculated using the ionized gas results [18, 19].

$$\mathbf{F} = \mathrm{e}\left(n_{\mathrm{i}} - n_{\mathrm{e}}\right)\mathbf{E} \tag{18}$$

$$q''' = Z_i \mathrm{e}\left(\boldsymbol{\Gamma}_{\mathbf{i}} \cdot \mathbf{E}\right) \tag{19}$$

In Eq. (19), the term on the RHS is the ion Joule heating, since only the heavy particles thermalize with the bulk gas. The ion Joule heating term usually has a thermalization factor that accounts for the fraction of energy that is locally equilibrated with the gas. In a xenon discharge at 100 (*Torr*), it was assumed by Boeuf, Pitchford, and Schoenbach [20] that only 25% of the energy was deposited in the neutral gas and the maximum gas temperature (~ 460 *K*) of their simulation matched relatively well with the gas temperature (~ 500 *K*) obtained from experiments. In this case, the ion Joule heating rapidly equilibrates with the gas since the ion-neutral mean free path is orders of magnitude smaller than the device length scale, a conservative approach is taken to obtain the upper bound for the gas heating, and the thermalization factor is assumed to be equal to one [19].

D. Ionized Gas Module Numerical Methodology

The system of governing equations for the plasma is solved using the semi-implicit, finite difference scheme module of the Multiscale Ionized Gas (MIG) code [7, 8]. The equations are solved decoupled starting with the steady Poisson equation, then the ion continuity equation, and the three metastable atoms continuity equations. The electron continuity and electron energy density equations are solved coupled with each other.

Poisson equation is approximated by combining the continuity equations of ions and electrons to predict the charge at present time step as

$$\nabla^2 \phi^{\mathrm{n+1}} = -\frac{\mathrm{e}}{\in_0}\left(n_{\mathrm{i}}{}^{\mathrm{n+1}} - n_{\mathrm{e}}{}^{\mathrm{n+1}}\right) \approx -\frac{\mathrm{e}}{\in_0}\left[n_{\mathrm{i}}{}^{\mathrm{n}} - n_{\mathrm{e}}{}^{\mathrm{n}} + \Delta t\left(\nabla \cdot \boldsymbol{\Gamma}_{\mathrm{e}}^{\mathrm{n}} - \nabla \cdot \boldsymbol{\Gamma}_{\mathrm{i}}^{\mathrm{n}}\right)\right] \tag{20}$$

The Poisson equation is solved using second order central difference scheme where the RHS is treated as a source since it depends on previous time step information.

$$\frac{\phi_{j+\Delta x}^{n+1} - 2\phi_j^{n+1} + \phi_{j-\Delta x}^{n+1}}{\Delta x^2} + \frac{\phi_{j+\Delta y}^{n+1} - 2\phi_j^{n+1} + \phi_{j-\Delta y}^{n+1}}{\Delta y^2} = S_j^n \tag{21}$$

The continuity equations for ions, electrons, and metastable atoms are solved using central difference on a staggered mesh and the volume source terms (S_{k}) are treated explicitly. The time discretization is first order implicit Euler method, beneficial for stability purposes.

$$\frac{\left(n_k\right)_j^{n+1}-\left(n_k\right)_j^n}{\Delta t}+\frac{\left(\Gamma_{k,x}\right)_{j+\Delta x/2}^{n+1}-\left(\Gamma_{k,x}\right)_{j-\Delta x/2}^{n+1}}{\Delta x}+\frac{\left(\Gamma_{k,y}\right)_{j+\Delta y/2}^{n+1}-\left(\Gamma_{k,y}\right)_{j-\Delta y/2}^{n+1}}{\Delta y}=\left(S_k\right)_j^n \tag{22}$$

The face fluxes are discretized using the first order accurate Scharfetter-Gummel scheme [21].

$$\begin{aligned}
&\left(\Gamma_{k,x}\right)_{j+\Delta x/2}^{n+1}=b_{j+\Delta x/2}^{n+1}\eta_{j+\Delta x/2}^{n+1}+\left(n_k\right)_j^{n+1}V_{x,j}\\
&\eta_{j+\Delta x/2}^{n+1}=\left(D_k\right)_{j+\Delta x/2}^{n+1}\left[\frac{\left(n_k\right)_j^{n+1}}{1-\exp\left(-\Delta x b_{j+\Delta x/2}^{n+1}\right)}+\frac{\left(n_k\right)_{j+\Delta x}^{n+1}}{1-\exp\left(+\Delta x b_{j+\Delta x/2}^{n+1}\right)}\right]\\
&b_{j+\Delta x/2}^{n+1}=\frac{\mathrm{sgn}(q_k)\left(\mu_k\right)_{j+\Delta x/2}^{n+1}E_{x,j+\Delta x/2}^{n+1}}{\left(D_k\right)_{j+\Delta x/2}^{n+1}}
\end{aligned} \tag{23}$$

The *k* subscript refers to the particle specie, the *j* to the node number, and the *n* superscript to the time-step. The electron energy density is solved in a similar manner, shown in Eq. (24), simultaneously with the electron continuity equation using a Newton-Raphson non-linear solver.

$$\begin{aligned}
&\frac{\left(n_\varepsilon\right)_j^{n+1}-\left(n_\varepsilon\right)_j^n}{\Delta t}+\frac{\left(\Gamma_{\varepsilon,x}\right)_{j+\Delta x/2}^{n+1}-\left(\Gamma_{\varepsilon,x}\right)_{j-\Delta x/2}^{n+1}}{\Delta x}+\frac{\left(\Gamma_{\varepsilon,y}\right)_{j+\Delta y/2}^{n+1}-\left(\Gamma_{\varepsilon,y}\right)_{j-\Delta y/2}^{n+1}}{\Delta y}\\
&+e\frac{\left[\left(\Gamma_{e,x}\right)_{j+\Delta x/2}^{n+1}+\left(\Gamma_{e,x}\right)_{j-\Delta x/2}^{n+1}\right]}{2}\frac{\left[\left(E_x\right)_{j+\Delta x/2}^{n+1}+\left(E_x\right)_{j-\Delta x/2}^{n+1}\right]}{2}\\
&+e\frac{\left[\left(\Gamma_{e,y}\right)_{j+\Delta y/2}^{n+1}+\left(\Gamma_{e,y}\right)_{j-\Delta y/2}^{n+1}\right]}{2}\frac{\left[\left(E_y\right)_{j+\Delta y/2}^{n+1}+\left(E_y\right)_{j-\Delta y/2}^{n+1}\right]}{2}\\
&+\frac{2m_e}{m_n}\nu_{en}\left[\left(n_\varepsilon\right)_j^{n+1}-\frac{3}{2}\left(n_e\right)_j^{n+1}k_B\left(T_{gas}\right)_j\right]=-e\sum_l\Delta E_l^e\left(r_l\right)_j^n
\end{aligned} \tag{24}$$

Each equation imposes a different restriction on the time step. The electric potential time step restriction is based on the Maxwell time [14], whereas the heavy species fluxes restriction depends on the *Courant-Friedrichs-Lewy* (*CFL*) condition. The time step restrictions imposed by the electrons and the argon chemistry are stricter than the heavy species transport restrictions. The electron and the chemical source terms time step restrictions depend on the *CFL* condition imposed by the electron energy transport. In all our simulations, all of the equations are advance at the most restrictive time step value from uniform initial conditions.

V. Rarefied Gas Module (RGM)

The numerical model for the argon gas flow in the thruster assumes that the gas is rarefied. The Knudsen number (*Kn*) is the ratio of mean free path length (λ) to a representative physical length scale such as the height of the channel (*H*) [22, 23].

$$Kn=\frac{\lambda}{H} \tag{25}$$

$$\lambda=\frac{1}{\sqrt{2}n\pi d^2}\cong\frac{16\mu}{5\rho\sqrt{2\pi RT}} \tag{26}$$

The mean free path length is a function of atomic diameter (d) and gas number density (n). Kn is used to determine which numerical modeling approach is more appropriate: statistical mechanics or continuum mechanics. As $Kn \to 0$, the flow is assumed sufficiently continuous, whereas for $Kn > 10$, the flow is assumed free-molecule. For $10^{-3} < Kn < 10$ the flow is neither sufficiently continuum nor completely molecular [24]. For this range, the flow is further divided into two subcategories: slip flow regime $10^{-3} < Kn < 10^{-1}$ and transitional regime for $10^{-1} < Kn < 10$ [24]. In our cases, Kn is in the slip regime by design. The Kn is 0.019 at the inlet of the thruster and higher for the outlet (~ 0.1).

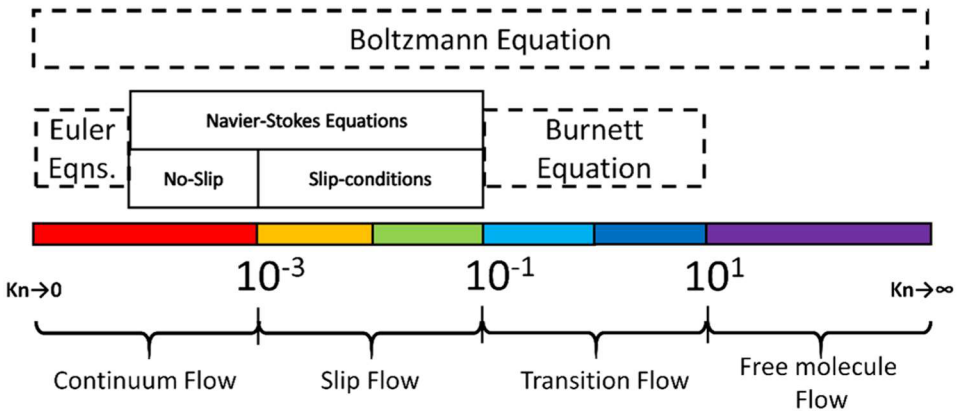

Fig. 2 Gas flow regimes depending on Kn [24].

As shown in Fig. 2, for the slip flow regime the flow is modeled with Navier-Stokes equations and slip-flow boundary conditions [24]. Maurer, Tabeling, Joseph, and Willaime [25] estimated the upper limit of the slip flow regime as $Kn = 0.3 \pm 0.1$ [26], where Kn is based on the channel height (H). For RGEJ, only the cases with ($Kn < 0.1$ or $Kn \sim 0.1$) will be presented and studied.

A. Rarefied Gas Governing Equations

In the rarefied gas simulation, a 2-D, time-dependent, density-based compressible flow Navier-Stokes equation system was used with the assumption of ideal gas using argon as the working fluid [24]. The continuity, momentum, and energy equations are given in Raju [24], with the additions of the terms containing (F_x, F_y, q''').

$$\frac{\partial \rho}{\partial t} + \frac{\partial (u\rho)}{\partial x} + \frac{\partial (v\rho)}{\partial y} = 0 \tag{27}$$

$$\begin{aligned}
&\frac{\partial u}{\partial t} + u\frac{\partial u}{\partial x} + v\frac{\partial u}{\partial y} + R\frac{\partial T}{\partial x} + \frac{RT}{\rho}\frac{\partial \rho}{\partial x} = \frac{F_x}{\rho} + \frac{1}{\rho}\left[\frac{4}{3}\frac{\partial}{\partial x}\left(\mu\frac{\partial u}{\partial x}\right) + \frac{\partial}{\partial y}\left(\mu\frac{\partial u}{\partial y}\right) - \frac{2}{3}\frac{\partial}{\partial x}\left(\mu\frac{\partial v}{\partial y}\right) + \frac{\partial}{\partial y}\left(\mu\frac{\partial v}{\partial x}\right)\right] \\
&\frac{\partial v}{\partial t} + u\frac{\partial v}{\partial x} + v\frac{\partial v}{\partial y} + R\frac{\partial T}{\partial y} + \frac{RT}{\rho}\frac{\partial \rho}{\partial y} = \frac{F_y}{\rho} + \frac{1}{\rho}\left[\frac{\partial}{\partial x}\left(\mu\frac{\partial v}{\partial x}\right) + \frac{4}{3}\frac{\partial}{\partial y}\left(\mu\frac{\partial v}{\partial y}\right) - \frac{2}{3}\frac{\partial}{\partial y}\left(\mu\frac{\partial u}{\partial x}\right) + \frac{\partial}{\partial x}\left(\mu\frac{\partial u}{\partial y}\right)\right]
\end{aligned} \tag{28}$$

$$\begin{aligned}
&\frac{\partial T}{\partial t} + u\frac{\partial T}{\partial x} + v\frac{\partial T}{\partial y} + \frac{RT}{c_v}\left[\frac{\partial u}{\partial x} + \frac{\partial v}{\partial y}\right] = \frac{1}{\rho c_v}\left[\frac{\partial}{\partial x}\left(\kappa\frac{\partial T}{\partial x}\right) + \frac{\partial}{\partial y}\left(\kappa\frac{\partial T}{\partial y}\right) + q'''\right] \\
&+ \frac{\mu}{\rho c_v}\left[\frac{4}{3}\left(\frac{\partial u}{\partial x}\right)^2 + \frac{4}{3}\left(\frac{\partial v}{\partial y}\right)^2 - \frac{4}{3}\left(\frac{\partial u}{\partial x}\right)\left(\frac{\partial v}{\partial y}\right) + \left(\frac{\partial v}{\partial x}\right)^2 + \left(\frac{\partial u}{\partial y}\right)^2 + 2\left(\frac{\partial v}{\partial x}\right)\left(\frac{\partial u}{\partial y}\right)\right]
\end{aligned} \tag{29}$$

The ideal gas constant (R) and the specific heat at constant pressure (c_v) are considered constant values, whereas the thermal conductivity (κ) and the viscosity (μ) are functions of the gas temperature [27]. The governing equations are written in the non-dimensional form using a velocity of 100 *m/s*, a length scale of 0.01 *m*, a pressure of 100 *Pa*, a temperature of 300 *K*, and density from the ideal gas law.

B. Rarefied Gas Boundary Conditions

The boundary conditions for the rarefied gas simulation are fixed stagnation density and temperature at the inlet ($\rho_0 = P_0/RT_0$, $T_0 = 300$ K, where $P_0 = 133.3$ Pa). Isentropic flow assumption is used to calculate the static density and temperature at the inlet plane. At the walls, there is no penetration (the normal velocity is equal to zero). At the outlet, static pressure is assumed to be ($P_{Out} = 0.05$ Torr) if Mach number is subsonic and ($\rho_{Out} = P_{Out}/RT_{Out}$), else ρ is extrapolated from internal nodes. Boundary conditions for a rarefied gas are used for tangential velocity at the wall face, as described by Maxwell [28], similar to Raju [24]. For example, for the top wall face inside the channel, the tangential velocity boundary condition is

$$-\frac{\mu}{\rho}\left(\frac{\partial u}{\partial y}\right)\Bigg|_{y=H/2} = \frac{5\sqrt{2\pi RT}}{16}\frac{\sigma_v}{(2-\sigma_v)}\left[u - \underbrace{\frac{3}{4}\frac{\mu}{\rho T}\left(\frac{\partial T}{\partial x}\right)\Bigg|_{y=H/2}}_{\text{Thermal Creep}}\right] \tag{30}$$

Since the cases are adiabatic, $\partial T/\partial x = 0$ or $\partial T/\partial y = 0$ is used as a temperature boundary condition at the wall. The tangential momentum accommodation coefficient ($\sigma_v = 0.89$ [29]) found in the formula of slip flow boundary condition is selected based on average values for argon interacting with different materials or it is picked based on the assumption that the particles reflect diffusely from the surface ($\sigma_v = 1.0$), depending on the case. The rest of the boundary conditions needed are zero flux normal to the edges of the domain [$\partial(...)/\partial x = 0$ or $\partial(...)/\partial y = 0$].

C. Rarefied Gas Numerical Methodology

The plasma numerical simulation is performed using the *ionized gas module* described in *Section IV*, whereas the rarefied gas numerical simulation is performed using the *rarefied gas module* described in *Section V*. The rarefied gas simulations are modeled using finite element methods and loosely coupled with the *ionized gas module* as shown in Fig. 1. The numerical simulation of the rarefied gas is performed using an existing, finite element based module in the Multi-scale Ionized Gas (MIG) [7, 8]. This module of MIG utilizes the Galerkin weak statement combined with the Newton-Raphson nonlinear solver. Bilinear elements are used in the *rarefied gas module* for the numerical analysis of the RGEJ thruster. In order to provide stability to the solution, the *streamline up-winding* (*SU*) artificial diffusion method in 2-D is used [30]. The MIG flow solver platform had been utilized for many different applications, including electric propulsion, micro-flows, nanoscale flows, fluid dynamics, and plasma physics [31-34]. Most recently, the finite difference *ionized gas module* has been added to extend MIG's capabilities.

VI. Geometry and Grid

The micro-thruster was designed with a long (20 *mm*), narrow (3 *mm*) slot to prevent the possibility of catastrophically plugging the thruster's throat. The absence of an expansion nozzle at the exit of the channel is due to predicted low Reynolds numbers ($Re < 100$) [6]. Since microsatellites require lower thrust and cannot operate at high enough plenum pressures, the operational Reynolds number for micro-nozzles may decrease to values as low as one hundred, and as heat is added, the flow experiences a further decrease in Reynolds number. Micro-thrusters with low throat Reynolds number ($Re < 100$) do not experience any gains from an expansion nozzle [35]. The low plenum-pressure operation condition is chosen to scale the thrust and for the additional benefit of reduced propellant storage pressure, therefore easing the propellant tank mass and valve leakage requirements [1].

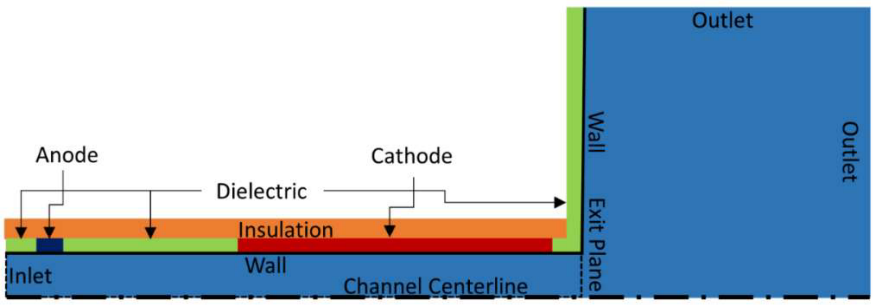

Fig. 3 Geometry and design of cases tested [6].

The domain region numerically simulated (light blue) is shown in Fig. 3. The *ionized gas module* models only the region inside the channel (0 *mm* < x < 20 *mm*), since the charged particle number densities are negligible at the exit plane. The mesh inside the channel has 401 nodes × 31 nodes. For the cases tested, the anode is between (1 *mm* < x < 2 *mm*) and the cathode (8 *mm* < x < 19 *mm*). The *rarefied gas module* models the channel region and the plume. The plume has 201 nodes × 201 nodes and is 10 *mm* × 10 *mm*. All cells are rectangular and have constant Δx and Δy. It is only necessary to solve one-half of the domain due to symmetry. The maximum value of the magnitude of the electron velocity ($\boldsymbol{v}_e = \boldsymbol{\Gamma}_e/n_e$) in the *IGM* (the plasma code) results is (~ 10^8 m/s), which for the given time step ($\Delta t = 5\times10^{-13}$ s) and mesh size ($\Delta x = \Delta y = 5\times10^{-5}$ m) produces a $CFL = \boldsymbol{v}_e \Delta t/\Delta x = 1.0$, which is within the stability regime ($CFL \leq 1$) for an explicit and therefore a semi-implicit numerical code. For the *RGM* (the gas code) results, the maximum value of the kinematic viscosity $\nu = \mu/\rho$ is ~ 0.667 m^2/s, which for the given time step (1×10^{-8} s) and mesh size ($\Delta x = \Delta y = 5\times10^{-5}$ m) produces a $CFL = \nu\,\Delta t/\Delta x^2 = 2.668$, which is around the maximum *CFL* value this implicit numerical scheme can withstand.

VII. Benchmarking/Validation

The rarefied gas module (the gas code) was verified using a plane Poiseuille flow case and its solution matched the analytical solution with L_1 and L_∞ norms of $\mathcal{O}(10^{-8})$. Additionally, a benchmarking of the rarefied gas module using results from Chen, Lee, and Sheu [36], which were validated within 1.15% accuracy with experimental results of Pong, Ho, Liu, and Tai [37], was performed previously in Blanco and Roy [6]. The case tested consists of a subsonic gas flow through a microchannel. The flow is in the slip flow regime. The maximum discrepancy between Chen, Lee, and Sheu [36] and the *rarefied gas module* result, in the x-component of velocity at the centerline, occurs at x = 2500 μm. This maximum discrepancy of 1.6 % can be attributed to the use of a different value of thermal conductivity and a different numerical scheme. The pressure discrepancy along the centerline is similar to the x-component of velocity discrepancy. Exact values for the pressure along the centerline are not given in Chen, Lee, and Sheu [36], therefore an exact comparison of the pressure was not performed. The temperature remains near constant throughout the domain ($T \sim T_{wall} = 314\ K$), and the y-component of velocity is close to zero. Overall, the *rarefied gas module* matched closely with results in literature.

The *ionized gas module* (the plasma code) was verified using the method of manufacturing solutions with the same procedure as in Houba [38]. Additionally, a simulation in 1-D of a parallel-plate, capacitively coupled, low-pressure, symmetric RF discharge driven at 13.56 MHz was performed and compared with Godyak, Piajak, and Alexandrovich [39]. Although the RGEJ cases in this study use a DC applied potential difference, the RF discharge experiment of Godyak, Piajak, and Alexandrovich [39] is employed for this validation since the numerical models used for RF and DC glow discharges are almost identical except for the applied alternating voltage in RF discharges. In previous studies, Sitaraman and Raja [19] and Deconinck [16] have successfully used the LMEA model to investigate an RF discharge thruster and a DC discharge thruster, respectively. The description of the validation case and the results were presented in Blanco and Roy [6]. The maximum percent error of the voltage amplitude in the range of interest for the peak-to-peak voltage (300 to 800 *V*) is 5.53% for γ_{sec} equal to 0.01, a reasonable error by drift-diffusion model standards. Drift-diffusion models typically have relatively large errors due to inaccuracies in the input coefficients as well as the model's inherent approximation of the Boltzmann equation. For example, the variation in the reduced mobility (μn_n) when using different collision cross-section libraries, in a Boltzmann solver such as BOLSIG+, for the electron mean energy (7-10 *eV*) region is of ~5% [40].

VIII. RGEJ Results

In Blanco and Roy [6], a comparison of cases with different voltages was presented, whereas in this study a comparison between cases with different tangential momentum accommodation coefficient is given. The total electrothermal heating source, total plasma-induced force, mass flow rate, thrust, specific impulse, specific impulse percent increase, shear force, current, and power are calculated using the following formulas.

$$\dot{Q} = 2\int_0^{H/2}\int_0^{L}(q''')Wdxdy, \text{ where W=1 cm} \tag{31}$$

$$\bar{F}_x = 2\int_0^{H/2}\int_0^{L}(F_x)Wdxdy \tag{32}$$

$$\dot{m} = 2\int_{0}^{H/2} (\rho u)\mathrm{W}dy \tag{33}$$

$$F_{\mathrm{Thrust}} = 2\int_{0}^{\mathrm{H}/2} (\rho\,\mathrm{u}^2 + \mathrm{P})\mathrm{W}dy \tag{34}$$

$$I_{sp} = \frac{F_{\mathrm{Thrust}}}{\dot{m}\mathrm{g}_0}, \text{ where } \mathrm{g}_0 = 9.81 \text{ m/s}^2 \tag{35}$$

$$I_{sp}\ \mathrm{Inc.} = \frac{\left(I_{sp} - I_{sp,\ base\ case}\right)}{I_{sp,\ base\ case}} \cdot 100 \tag{36}$$

$$F_{\tau_{\mathrm{Wall}}} = 2\int_{0}^{\mathrm{L}} (\tau_{\mathrm{Wall}})\mathrm{W}dx, \text{where } \tau_{\mathrm{Wall}} = -\mu \left.\frac{\partial u}{\partial y}\right|_{y=\mathrm{H}/2} \tag{37}$$

$$I = 2\int_{\mathrm{L_{Electrode}}} \left(\sum_{\mathrm{k}} Z_k e \Gamma_{\mathrm{k}} \cdot \hat{\mathrm{n}}\right) \mathrm{W}dx \tag{38}$$

$$P_W = VI \tag{39}$$

The following table shows the performance parameters of a cold gas thruster case (*base case*) with the given geometry and boundary conditions (using $\sigma_v = 0.89$) previously explained, and two different plasma-aided cases operating at a voltage difference of 750 *V*. The main difference between the plasma-aided cases is the value of the tangential accommodation coefficient (σ_v) with *case 750V* having a $\sigma_v = 0.89$ and *case 750V-2* having a $\sigma_v = 1.00$.

Table 1. *Values of: voltage (V), mass flow rate ($\dot{m}$), thrust (F_{Thrust}), shear force ($F_{\tau_{Wall}}$), specific impulse (I_{sp}), specific impulse percent increase (I_{sp} Inc.), current (I), total electrothermal heating source (Q), power deposited (P_W), and fraction of the power deposited converted into electrothermal heating source (Q/P_W). STP means standard temperature (273.15 K) and pressure (100000 Pa).*

Case	V	$\dot{m}$	F_{Thrust}	$F_{\tau_{Wall}}$	I_{sp}	I_{sp} Inc.	I	Q	P_W	Q/P_W
	(V)	(SCCM)	(mN)	(mN)	(s)	(%)	(mA)	(mW)	(mW)	(%)
Base case	0	180.3	2.288	1.955	44.1	-	0.000	0	0	-
Case 750V	750	105.6	1.843	2.308	60.7	37.6	0.541	400	406	98.5
Case 750V-2	750	99.6	1.777	2.372	62.0	40.7	0.522	385	392	98.4

The specific impulse of *case 750V* (I_{sp} = 60.7 *s*) is 16% higher than the I_{sp} of a highly optimized argon propellant cold gas thruster (52 *s*) and 35% higher than the I_{sp} of the argon propellant FMMR (45 *s*) [1]. The increase in I_{sp} for *case 750V* over cold gas thrusters is achieved with only 406 (*mW*) per centimeter of width of the device and 98.5% of the power deposited is converted to heating of the neutral gas. This percentage is higher than the range (81-95%) predicted by Houba and Roy [14] for a device operating at an assumed constant temperature (300 *K*) and a pressure (0.6 *Torr*) using air as the working fluid. The remainder of the discharge power goes into the electrons, which lose energy in inelastic collisions due to the various ionization, attachment, and excitation reactions [14]. The specific impulse increase of *case 750V-2* is 1.3% higher than *case 750V*. This small increase is caused by a 12.4% increase in the tangential momentum accommodation coefficient (σ_v). In literature, the σ_v values have been measured in

experiments from a high of about 1.2 to a low of about 0.2, but these extremes are not typical and the majority of the experimental measurements are in the 1.06 to 0.85 range [41]. An increase in the σ_v value affects the I_{sp} of the thruster in a minor manner, but the resulting increase in I_{sp} is accompanied by a decrease in power consumption of 3.4%. In order to understand how the increase in σ_v affects the behavior of the gas and plasma flow in the thruster, the results for the different cases are shown and compared with each other.

The following figures show a comparison of the results of the rarefied gas simulations for the *base case* (with $\sigma_v = 0.89$), *case 750V* (with $\sigma_v = 0.89$), and *case 750V-2* with higher tangential momentum accommodation coefficient ($\sigma_v = 1.0$).

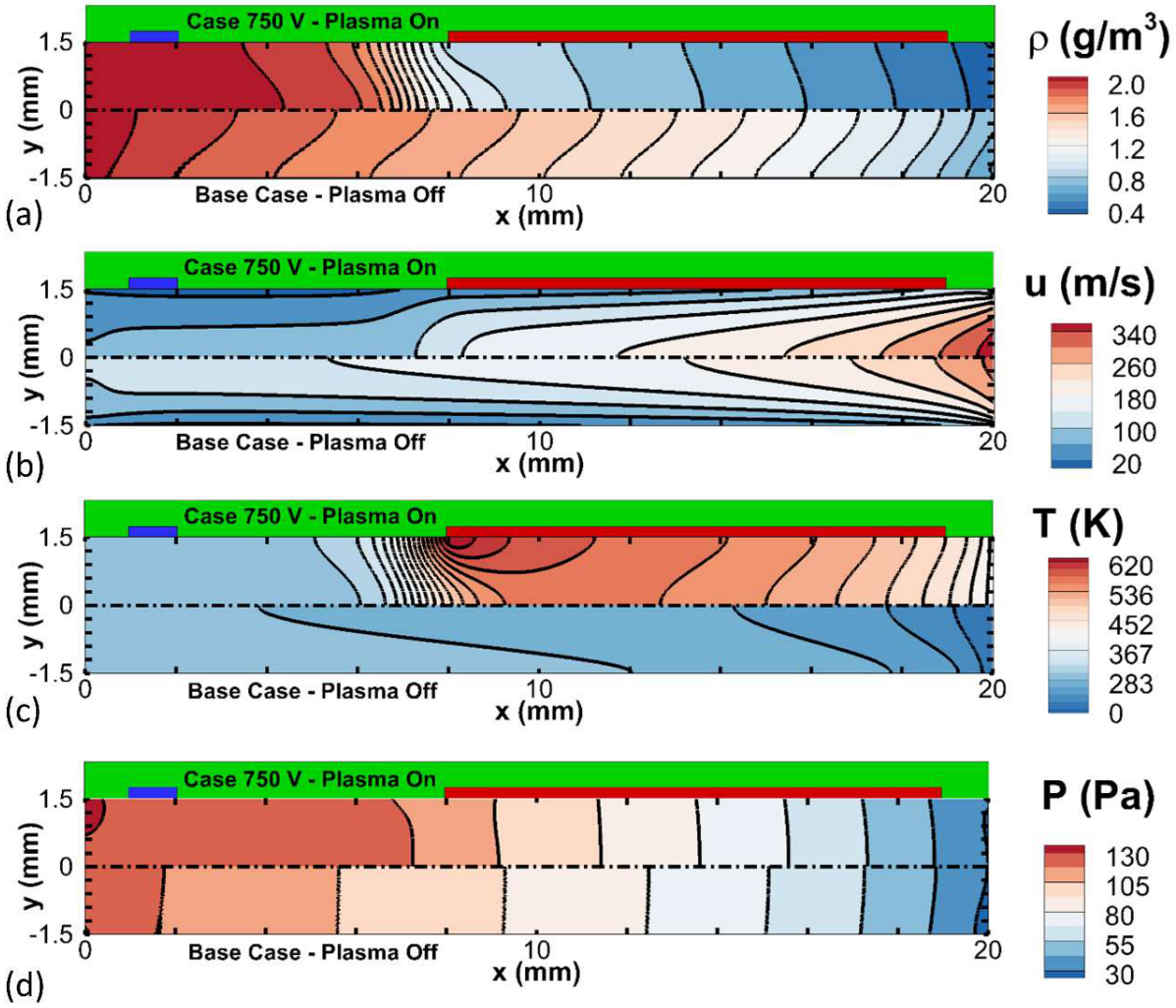

Fig. 4 Comparison of rarefied gas results for the *base case* and *case 750V*. The variables compared are a) density, b) x-component of velocity, c) temperature, and d) pressure. The top dielectric wall (in green) is shown with the position of the anode electrode (in blue) and the cathode electrode (in red).

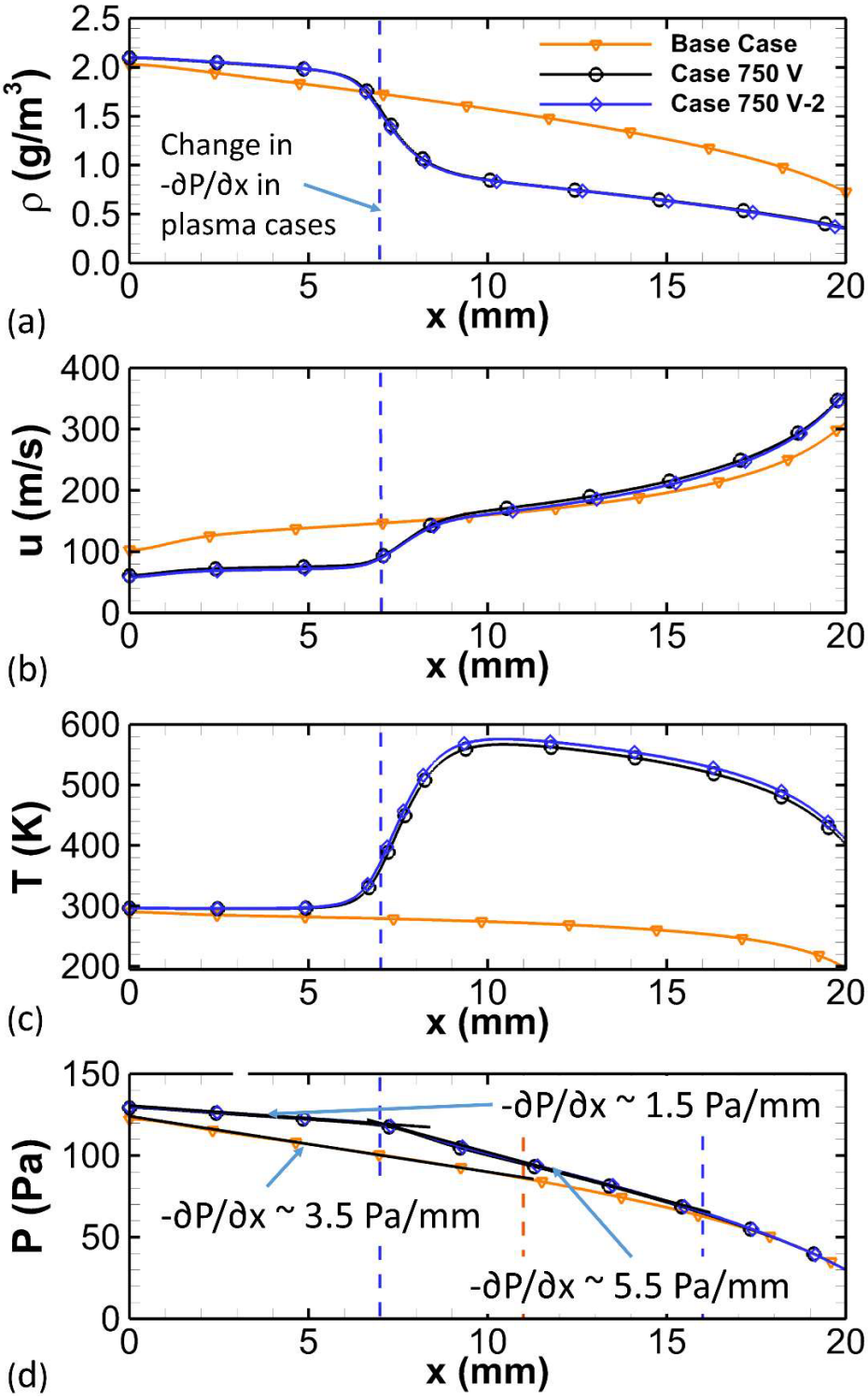

Fig. 5 Comparison of rarefied gas centerline results for the *base case*, *case 750V*, and *case 750V-2*. The variables compared are a) density, b) x-component of velocity, c) temperature, and d) pressure.

In Fig. 4(c), the volumetric plasma-induced electrothermal heating source (q''') locally heats the gas in *case 750V* to temperatures as high as (~ 640 *K*) near the corner of the cathode electrode where the high electric field causes the q''' to increase sharply. By comparison, the *base case* has a temperature profile that decreases along the x-axis direction as we approach the exit plane due to the flow expansion. In Fig. 5(c), the exit temperature at the centerline

is higher for *case 750V* and *case 750V-2* than for the *base case*, each having a temperature of (~ 400 *K*), twice the value of the *base case* (~ 200 *K*). The speed of sound doubles for the plasma-aided cases operating at 750 *V*. The difference between *case 750V* and *case 750V-2* in Fig. 5(c) cannot be clearly observed, but the higher σ_v and resulting shear stress in *case 750V-2* causes higher temperature values along all the centerline with a maximum difference of 9 *K* between the profile of each plasma-aided case.

The pressure profile, see Fig. 4(d) and Fig. 5(d), is affected by the addition of thermal energy to the flow. The *base case* shows a near linear decrease in pressure for (x < 11 *mm*) with $(-\partial P/\partial x) \sim 3.5$ *Pa/mm*, followed by a parabolic decrease. Four important effects are encountered in micro-flows: *rarefaction*, *compressibility*, *viscous heating*, and *thermal creep* [26]. In the cases presented, the *viscous heating* effect is not apparent since for pressure-driven compressible flows the expansion cooling negates it [26]. Out of those, *compressibility* and *rarefaction* are competing effects. The curvature in the pressure distribution of compressible flows is due to *compressibility* effects, the higher the Mach number the greater this effect becomes, the curvature increases with an increased of the inlet-to-outlet pressure ratio [26]. *Rarefaction* decreases the curvature in the pressure distribution, which becomes increasingly linear as the free-molecular flow regime is approached with increasing *Kn* numbers [26]. In the pressure profile in Fig. 5(d), *rarefaction* is dominant in the *base case* for (x < 11 *mm*) and the *compressibility* effects become increasingly important in the rest of the domain due to increasing Mach number. For the plasma-aided cases, *case 750V* and *case 750V-2*, the pressure profile is very similar, but the pressure profile has two distinct linear regions, one before and one after the area where thermal energy is deposited. The effect of *rarefaction* dominates for (x < 16 *mm*) due to the higher *Kn* numbers found in these cases in comparison to the *base case*. For the plasma-aided cases, the two distinct linear regions have $(-\partial P/\partial x) \sim 1.5$ *Pa/mm* for (0 *mm* < x < 7 *mm*) and 5.5 *Pa/mm* for (7 *mm* < x < 16 *mm*), respectively. These two different regions are caused by the difference in temperature, which affects the shear stress at the wall.

If the *thermal creep*, which is a *rarefaction* effect, is neglected in Eq.(30) for simplicity of the analysis, the shear stress is proportional to ρ, u, and $T^{0.5}$ at the wall. Since the mass flow rate requirement is smaller for the plasma-aided cases than for the *base case*, the mass flux (ρu) is smaller in most of the domain along the wall for the plasma-aided cases. Alternatively, the shear stress increases with the square root of temperature ($T^{0.5}$) as observed in Eq.(30). These two competing contributions, (ρu) and ($T^{0.5}$), cause the shear stress to decrease before the region where Q is added and increase right after. The *thermal creep* plays a smaller role in the cases presented that increases this effect since molecules creep from cold towards hot regions [26]. The *thermal creep* contribution to the shear stress is negative whereas T is increasing and positive whereas T is decreasing along the tangential direction at the wall.

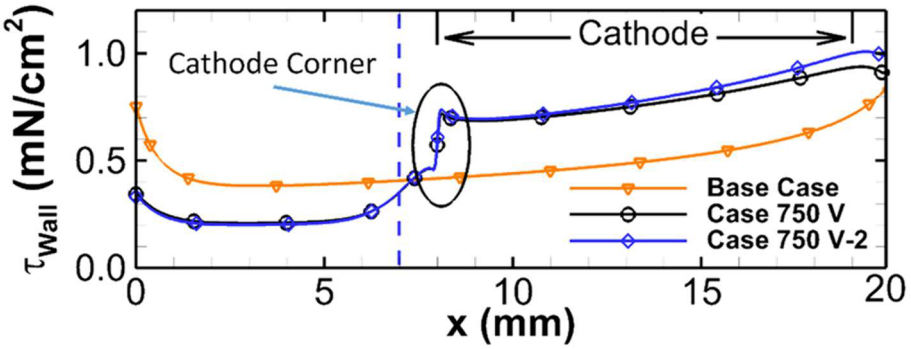

Fig. 6 Shear stress at the wall.

As shown in Fig. 6, the *thermal creep* plays a significant role close to the cathode electrode corner at (~ 8 *mm*) where the magnitude of $\partial T/\partial x$ is the highest, causing a sharp discontinuity in the profile of shear stress at the wall. In this location, the shear stress abruptly increases due to the *thermal creep*, but the *thermal creep* effect is negligible in the rest of the domain due to low $\partial T/\partial x$ values. The total shear force experienced by the fluid and the thrust produced by the device depends on the fraction of the wall area that is exposed to the higher temperatures. In *case 750V-2*, the factor $[\sigma_v/(2-\sigma_v)]$ multiplying Eq.(30) is higher (= 1.0) than for the *base case* and *case 750V* (= 0.8), increasing the shear stress along the wall.

The x-component of velocity (u) plots, in Fig. 4(b) and Fig. 5(b), show the effect of having two distinct $(-\partial P/\partial x)$ regions in the plasma-aided cases. The *base case* has a constant acceleration of the flow along the channel, but *case 750V* and *case 750V-2* have approximately constant u-velocity component before thermal energy is added due to the low $(-\partial P/\partial x)$ for (x < 7 *mm*) follow by an acceleration region where $(-\partial P/\partial x)$ is higher. The acceleration region

is similar to a shorter channel operating with the same inlet to outlet pressure ratio at a higher inlet temperature. This observation may be useful to modify the geometry of the thruster's design in the future for optimization purposes.

The addition of thermal energy increases u at the exit plane centerline from 311 (*m/s*) in the *base case* to 362 (*m/s*) in *case 750V* and decreases the density from 0.73 (g/m^3) to 0.36 (g/m^3), see Fig. 4 (a) and Fig. 5(a), increasing the I_{sp} of the thruster.

Due to the higher shear stress at the wall over the entire channel length, *case 750V-2* has lower u at any given point in the domain than *case 750V*. The lower u values in *case 750V-2* causes the static pressure to be higher (7 *Pa* higher) at the inlet than *case 750V*, but due to the greater amount of friction at the wall, the flow is expanded to almost the same static pressure at the exit plane (only 0.16 *Pa* lower for *case 750V-2* than for *case 750V*). The density behaves in a similar manner for these two cases as their pressure profile.

Given that $\dot{m} \propto (\rho u)_{Exit}$, $F_{Thrust} \propto (\rho u^2 + P)_{Exit}$ and $I_{sp} \propto [u + P/(\rho u)]_{Exit}$, the mass flow rate and thrust decrease as ρ_{Exit} or u_{Exit} decreases, but the behavior of the I_{sp} is more complicated. Since the density at the exit plane is a lot lower (~ 51% and ~52%) for the plasma-aided cases than for the *base case* and the velocity at the exit plane for the plasma-aided cases is only ~16% and ~15% higher than the *base case*, both the mass flow rate and the thrust are lower for the plasma-aided cases. Conversely, their I_{sp} is higher than the *base case*, primarily due to the contribution of the $[P/(\rho u)]_{Exit}$ term, which increases with the large decrease in ρ_{Exit} since P_{Exit} is nearly constant for all three cases. It is also obvious that *case 750V* most have higher mass flow rate and thrust than *case 750V-2*, since the latter has lower ρ_{Exit} and u_{Exit}. In spite of this, the I_{sp} of *case 750V-2* is the highest, the lower values of ρ_{Exit} and u_{Exit} increase the $[P/(\rho u)]_{Exit}$ term enough to counteract the losses in I_{sp} due to the lower u_{Exit} term. The increase in shear stress at the wall helps to expand the flow in a more efficient manner. The cases studied show that a shear stress increase can be due to a higher temperature at the wall or to a higher tangential momentum accommodation coefficient. It is important to emphasize that due to low Reynolds numbers (< 30) in these cases and dominant viscous terms, no shock discontinuities are found in any of the results.

The following figures, Fig. 7 and Fig. 8, show the results of the ionized gas (the plasma) simulations for *case 750V* and case *750V-2*. The applied DC voltage difference of 750 V is within the operating conditions of the validation cases. Fig. 7(a-c) and Fig. 8 (a-c) display a comparison of the contours for the electrons number density, positive ions number density, and electron energy density with their higher values right before the cathode fall region. For *case 750V* the maximum values reach 4.03×10^{16} (m^{-3}), 4.23×10^{16} (m^{-3}), and 0.045 (J/m^3), respectively. The metastable atoms number densities, not shown, are approximately one to two orders of magnitude lower than the charged particles and their contribution to ionization is very small for the given pressure operation regime. The electron temperature (T_e), calculated using the electron energy and number densities, is (~ 4 eV) in the plasma column for both cases. In the cathode fall, where electron number density decreases to very small values (< 10^{13} m^{-3}) by comparison to the peak value (~ 10^{16} m^{-3}), the T_e is over-predicted and can increase exponentially in this region of vanishing electron density due to a numerical artifact of the fluid model [18]. This behavior of T_e does not affect the accuracy of the simulations for the other variables since the electron energy content is negligible in this part of the domain [18].

In Fig. 7(f) and Fig. 8 (f) the x-component of the volumetric plasma-induced electrostatic force is shown. Although the direct contribution of the force to the total thrust is negligible, the plasma-induced force terms (F_x, F_y) near the cathode corners are about a tenth of the pressure gradient terms ($-\partial P/\partial x$, $-\partial P/\partial y$) in the Navier-Stokes equation system. F_x and F_y locally affect the flow by creating a low-pressure region that pulls the flow towards the wall upstream of the corner of the cathode and accelerates the flow right after, in the tangential direction. The total plasma-induced force produced in the tangential direction ($\bar{F}_x$) is 38 ($\mu N/cm$), by comparison, the plasma force produced by Houba and Roy [14] is 5 ($\mu N/cm$) at 600 (V) and 0.6 ($Torr$) using air as the working fluid.

In Fig. 7(g) and Fig. 8 (g) the volumetric plasma-induced electrothermal heating source is shown, it is concentrated in the cathode fall, reaching a maximum value of 400 ($W\,cm^{-3}$) near the corner of the cathode for *case 750V*. Although this value looks large, it is concentrated in a small region of the domain and the net value of the total thermal heating source (Q) is $\mathcal{O}(100\ mW)$.

Most of the ionization happens close to edge of the plasma column before reaching the cathode fall and it is concentrated around the centerline. The ions flow from this region of high electric potential, but low electric field, to the walls where they recombined. In contrast, the electrons flow from the cathode to the rest of the walls, most of them flow into the anode and the rest into the dielectric sections of the walls to balance the ion current. The number of ions leaving the thruster through the exit plane is negligible; therefore, their contribution to the thrust is neglected. Some power is always lost through inelastic collisions to solid walls and the outflow, but the heating of the walls due to neutralization is not taken into account since our assumption of adiabatic walls is just an approximation to simplify the numerical simulation of a well-insulated thruster.

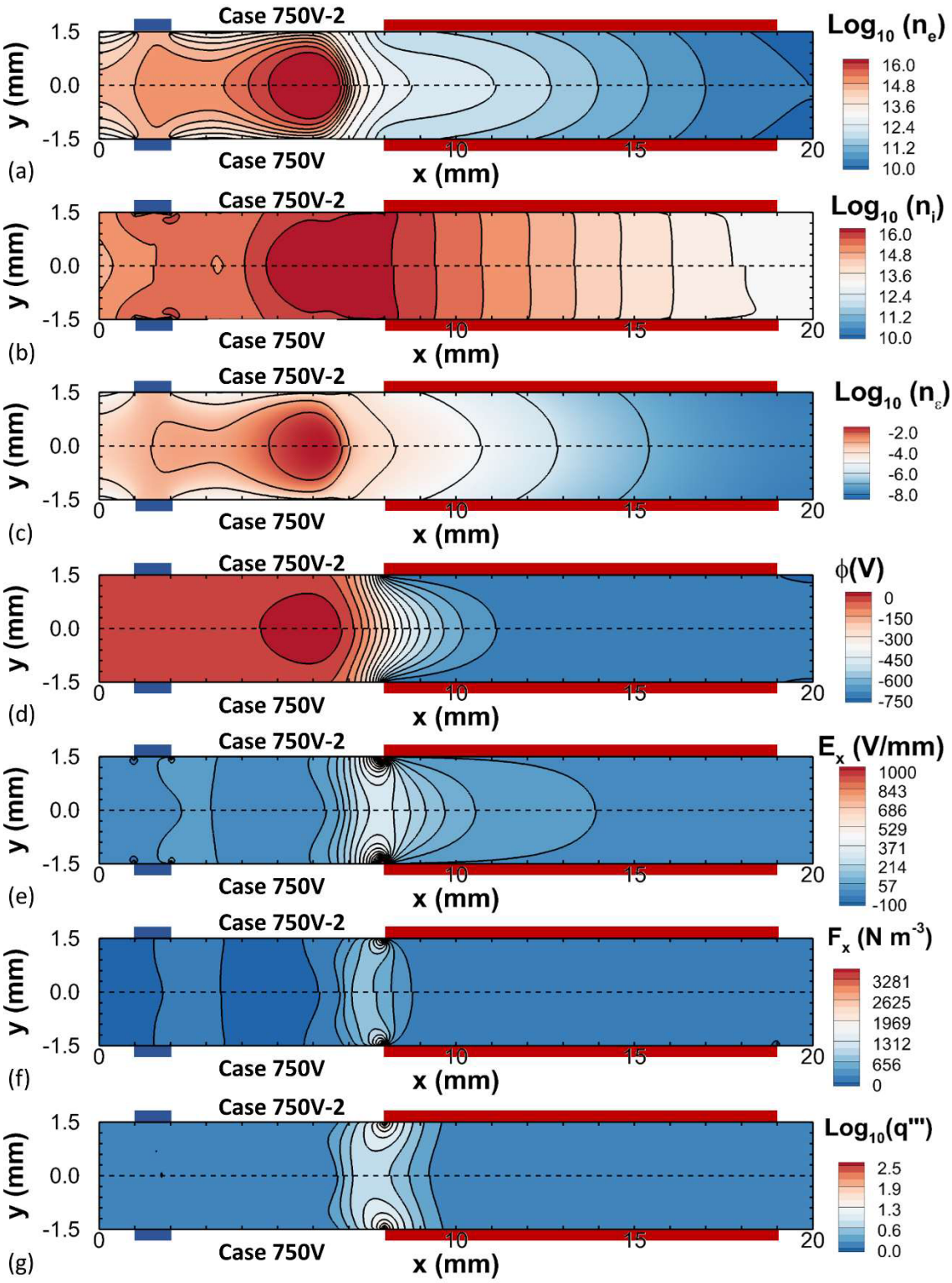

Fig. 7 Plasma discharge results for *case 750V* and *case 750V-2*. The variables compared are a) electron number density, m^{-3}, b) ion number density, m^{-3}, c) electron energy density, $J\ m^{-3}$, d) electric potential, V, e) x-component of the electric field, $V\ mm^{-1}$, f) volumetric plasma-induced electrostatic force, $N\ m^{-3}$, and g) x-component of the volumetric plasma-induced electrothermal heating source, $W\ cm^{-3}$. The position of the anode electrode (in blue) and the cathode electrode (in red) is shown on the top and bottom.

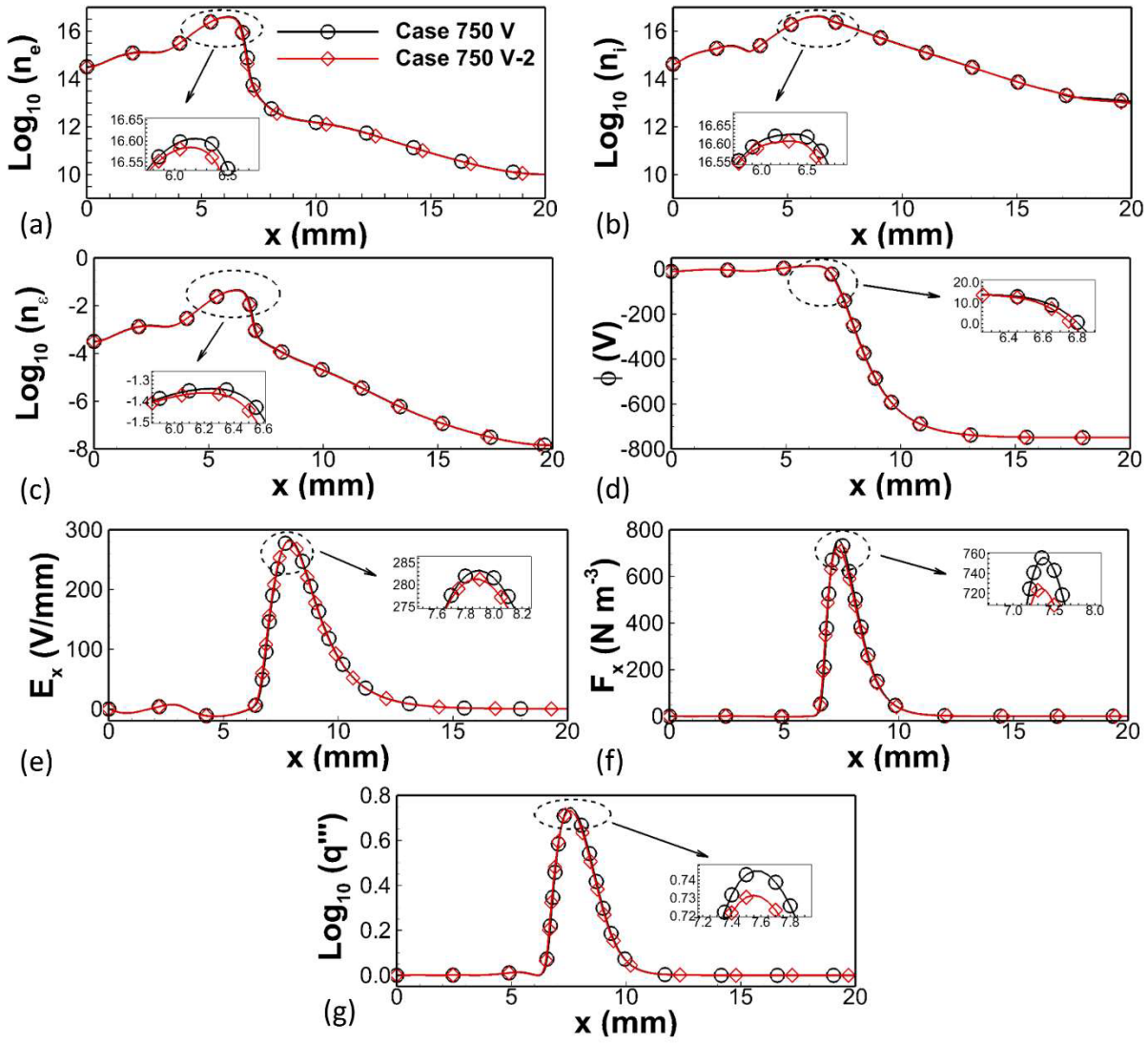

Fig. 8 Plasma discharge centerline results for *case 750V* and *case 750V-2*. The variables compared are a) electron number density, m^{-3}, b) ion number density, m^{-3}, c) electron energy density, $J\ m^{-3}$, d) electric potential, V, e) x-component of the electric field, $V\ mm^{-1}$, f) x-component of the volumetric plasma-induced electrostatic force, $N\ m^{-3}$, and g) volumetric plasma-induced electrothermal heating source, $W\ cm^{-3}$.

At first glance, *case 750V* and case *750V-2* look identical, but upon closer inspection the effect of the slightly higher gas temperature and lower gas density values in *case 750V-2* becomes obvious. The maximum values for each of the plasma variables are lower for *case 750V-2* and the location is further upstream than for *case 750V*. This phenomenon is consistent with the observation in Blanco and Roy [6], where for the higher voltage cases, with higher gas temperature, experience lower currents due to a decrease in the ion flux at the cathode. The ion flux decreases due to the increase in the ion diffusion in comparison to the ion mobility. Since *case 750V-2* has lower current due to the higher gas temperatures and the same voltage difference as *case 750V*, it operates with a lower power requirement than *case 750V*. The higher tangential momentum accommodation coefficient is beneficial to increase the I_{sp} and serves to illustrate the effect of shear stress at the wall on the performance of the RGEJ thruster.

Since the mass flow rate and thrust decrease for the plasma-aided cases, a longer width (W_{new}) is assumed for the given case to match the mass flow rate of the *base case* in order to calculate the thrust effectiveness and total efficiency. The thrust of the *base case* is subtracted from the thrust of the given case to take into account only the additional thrust produced by the formation of the plasma at the mass flow rate of the *base case*. The width ratio between the given case and the *base case*, the thrust effectiveness, and the total efficiency are defined by the following equations.

$$R_W = \left(\frac{W_{new}}{W}\right) = \left(\frac{\dot{m}_{\text{Base Case}}}{\dot{m}_{\text{Case}}}\right), \text{ where W=1 cm} \tag{40}$$

$$\zeta_{Thrust} = \frac{R_W \left(F_{Thrust}\right)_{\text{Case}} - \left(F_{Thrust}\right)_{\text{Base Case}}}{R_W \left(P_W\right)_{Case}} \tag{41}$$

$$\eta_T = \frac{\left(R_W \left(F_{Thrust}\right)_{\text{Case}} - \left(F_{Thrust}\right)_{\text{Base Case}}\right)^2}{2\left(\dot{m}_{\text{Base Case}}\right)\left(R_W\right)\left(P_W\right)_{\text{Case}}} \tag{42}$$

The thrust effectiveness and total efficiency for *case 750V* and *case 750V-2* are (1240 $\mu N/W$ and 10%) and (1311 $\mu N/W$ and 11.5%), respectively. For comparison, other electrothermal thrusters using plasma-aided technology such as the MPT [16, 18] operating at 100 *Torr* plenum pressure and a wall temperature of 300 *K*, produce a thrust effectiveness and total efficiency calculated with Eq. (40) to (42) of (50 $\mu N/W$ and 0.6%).

IX. Thermal Analysis

A simple thermal analysis of the thruster was performed by taking the temperature distribution at the channel walls and exit walls for *case 750V* obtained with adiabatic walls assumption to calculate the hypothetical heat loss through conduction and radiation. The analysis is performed in a similar manner as in Blanco and Roy [6], but a new design is investigated to insulate the thruster.

The heat loss via conduction is a minimum for thruster's slots that are stacked next to each other, similarly to FMMR. In the following conduction analysis, the heat loss via conduction is investigated for a single thruster's slot.

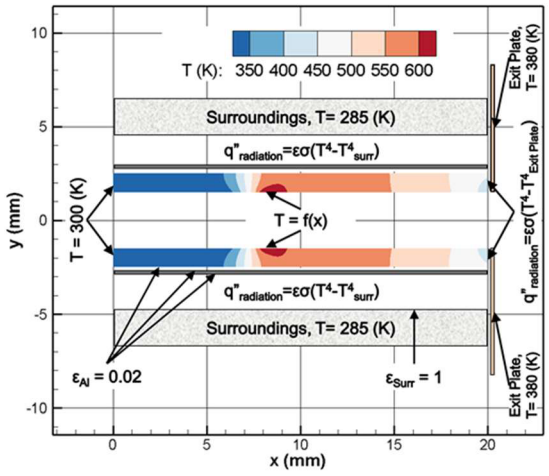

Fig. 9 Conduction heat loss analysis for *case 750V* assuming a width of 1 cm, with the temperature distribution given along the wall as T=f(x).

In Fig. 9, the conduction analysis of the thruster is performed using a (401×101) mesh, assuming 1.0 *mm* thick, insulating walls made of silica aerogel with a thermal conductivity of 4.2 *mW/(m·K)* for pressures (< 10 *Torr*). The thruster is covered with an aluminum layer and an additional aluminum thin layer separates the thruster from the surroundings. For a well-insulated satellite, a MEMS thruster system external average temperature is 285 *K* [42]. The exit plate is the external wall of the small satellite. At steady state operation conditions, the rarefied gas module predicts an average temperature of 380 *K* for the exit plate surface close to the thruster's exit plane. A thin gap separates the thruster walls from the exit plate to prevent heat loss via conduction through that side of the channel walls. Neglecting the thermal resistivity of the electrode and dielectric materials due to their thinness, and neglecting any heat loss due to radiation through the exit plate, due to their assumed low emissivity, the average heat loss through conduction of the internal walls at *T*=f(x) is 0.23 *mW* per centimeter of width of the thruster.

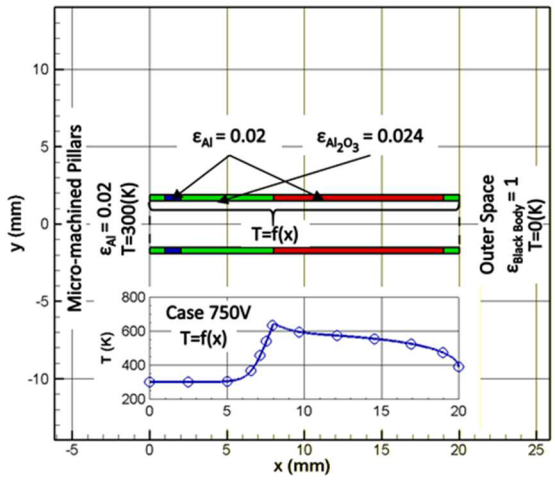

Fig. 10 Radiation heat loss analysis for *case 750V* assuming a width of 1 cm, with the temperature distribution of given along the wall as T=f(x).

In Fig. 10, the radiation analysis was performed using 400 plates on each internal wall, assuming each is a diffuse-grey surface. The inlet plane is considered a diffuse-grey surface with the emissivity of the electrodes since the plenum chamber will contain micro-machined pillars or a porous metal material to heat the propellant with residual heat. The radiation analysis has shown that if micro-machined pillars or a porous metal material is not used in the inlet, then a significant amount of thermal energy would scape the walls into the plenum, which would heat the gas in a non-localize manner. The background radiation temperature of outer space is assumed to be 0.0 *K*. The emissivities of the dielectric and electrodes were assumed to be $\varepsilon_{Al_2O_3} = 0.24$ (aluminum oxide) and $\varepsilon_{Al} = 0.02$ (aluminum), respectively [43]. The heat loss due to radiation is 30.1 *mW* per centimeter of width of the thruster. The radiation heat loss depends strongly on the emissivity of the internal walls.

The adiabatic assumption in the cases presented is intended to provide an upper limit for the thruster's performance for the given operational parameters. The overall heat loss of a thruster working in outer space is 30.34 *mW*, which is 7.5% of the input power in *case 750V*, depending on the internal temperature of the small satellite, the insulation layer of the thruster, and the emissivity of the internal walls. In laboratory conditions, with an environment temperature of 300 *K*, the heat loss through conduction would be negligible in a well-insulated thruster and the heat loss through radiation would be 23.9 *mW*, which is 5.9% of the input power, making the assumption of adiabatic walls a reasonable approximation for a comparisons with experiments. It is important to indicate that 1.5% of the total power in *case 750V* is not transferred to the gas and it is mostly lost to the walls in the form of heat (98.5% of the total power is transferred to the gas). This loss is expected to decrease the discrepancy between the adiabatic assumption cases and future results of experiments even further.

X. Conclusion

The RGEJ thruster, for *case 750V*, shows encouraging results with an improvement in I_{sp} of 37.6% over cold gas thrusters with the same geometry and working parameters, an improvement in I_{sp} of 16% over optimized argon propellant cold gas thrusters, and an improvement in I_{sp} of 35% over argon propellant FMMR. For the configuration of electrodes studied and this voltage, the majority of the energy is converted into gas heating (~ 98%); the plasma force plays a negligible role in the injection of momentum, but causes a localized effect near the corner of the cathode. *Case 750V-2* revealed that a higher tangential momentum accommodation coefficient is beneficial to increase the I_{sp}, the thrust effectiveness, and the total efficiency, but for the given increase in tangential momentum accommodation coefficient of 12.4% the improvements are small. Nonetheless, *case 750V-2* revealed that the surface roughness of the walls could play an important function in the optimization of the thruster.

High heat loss is typical in MEMS-scale micro-thrusters [1]. For example, FMMR required twice (200% of) the power used to heat the gas to operate due to heat losses. In contrast, a simple thermal analysis estimated that the proposed RGEJ thruster would require 7.5% more input power to maintain the same performance due to heat loss in outer space. This number could be further decreased by reducing heat loss through conduction and radiation by stacking many thrusters' slots and using a dielectric material with lower emissivity.

The RGEJ material compatibility between the propellant and the surface when operating with argon is not optimum because this propellant causes high sputtering, but if RGEJ can operate with water propellant, the long aluminum cathode electrodes could be silver plated to help mitigate the formation of hydrogen peroxide, serving as a catalyst to decompose it. Due to the low plenum pressure and the long slot design, RGEJ is expected to have very low or negligible valve leakage problems and no passage clogging complications that could result in a single-point failure. The system reliability and durability has to be determined, but the only real concern would be the electrode erosion due to sputtering, which is the most damaging in the front corner of the cathode electrodes. Due to the RGEJ design simplicity, with no moving parts, other reliability and durability problems are avoided. The RGEJ can even operate as a cold gas thruster. The RGEJ produces thrust in the $\mathcal{O}(mN)$ necessary for slew maneuvers at very low power. The minimum impulse bit of the RGEJ should be ($< 50\ \mu N{\cdot}s$).

If liquid or solid propellant is used, the weight and storage density of the propulsion system could be greatly reduced due to a reduction in the tank mass [1]. The storage density of the propellant is important to minimize the volume required for propellant tanks. The RGEJ design can be developed using simple MEMS fabrication techniques and common materials, which results in low-cost batch fabrication. The efficiency of the RGEJ is low (~ 10%, for *case 750V*), but higher than other electrothermal thrusters using plasma-aided technology (e.g., 0.6% for the MPT [16, 18]). The working principle of the RGEJ has been tested and the device has shown promising results that indicate its potential for real-world applications as a micro-propulsion thruster for small satellites. Further investigation is needed to optimize and improve the thruster.

Acknowledgments

This work was supported by the Space Research Initiative (SRI) program, a joint program between the University of Central Florida and the University of Florida. The authors would like to thank all members of the SRI project that collaborated to its success and both universities for their support.

References

[1] Micci, M. M., and Ketsdever, A. D., *Micropropulsion For Small Spacecraft, Reston*, American Institute of Aeronautics and Astronautics, Virginia, 2000.

[2] Ketsdever, A., Green, A., Muntz, E. P., and Vargo, S.,"Fabrication and Testing of the Free Molecule Micro-Reistojet: Initial Results," In 36th AIAA/ASME/SAE/ASEE Joint Propulsion Conference and Exhibit, Huntsville, AL, 2000, p. 3672.

[3] Ketsdever, A. D., Wadsworth, D. C., and Muntz, E. P., "Predicted Performance and System Analysis of the Free Molecule Micro-Resistojet," In Micropropulsion for Small Spacecraft, AIAA, Reston, VA, 2000, pp. 178-179.

[4] Soni, J., "Characterization of Plasma Actuator Based Microthruster Concepts for High Altitude Aircrafts and Cubsats," Ph.D. Dissertation, Mech. and Aero. Eng. Dept., University of Florida, Gainesville, FL, 2014.

[5] Roy, S., U.S. Patent for a "Method and Apparatus of Small Satellite Propulsion," US2012-0304618, publication date 6 December 2012.

[6] Blanco, A., and Roy, S., "Rarefied gas electro jet (RGEJ) micro-thruster for space propulsion," Journal of Physics D: Applied Physics, Vol. 50, No. 455201, 2017, pp. 1-15.

[7] Roy, S., "Combining Galerkin Matrix Perturbation with Taylor Weak Statement Algorithms," Computer Method in Applied Mechanics and Engineering, Vol. 184, 2000, pp. 87-98.

[8] Balagangadhar, D., and Roy, S., "Design Sensitivity Analysis and Optimization of Steady Fluid-Thermal Systems," Computer Methods in Applied Mechanics and Engineering, Vol. 190, 2001, pp. 5465-5479.

[9] Rafatov, I., Bogdanov, E. A., and Kudryavtsev, A. A., "On the accuracy and reliability of different fluid models of the direct current glow discharge," Physics of Plasmas, Vol. 19, 2012, p. 033502.

[10] Boeuf, J., and Pitchford, L., "Two-dimensional model of a capacitively coupled rf discharge and comparisons with experiments in the Gaseous Electronics Conference reference reactor," Physical Review, Vol. E 51, 1995, p. 1376.

[11] Rafatov, I., Bogdanov, E. A., and Kudryavtsev, A. A., "Account of nonlocal ionization by fast electrons in the fluid models of a direct current glow discharge," Physics of Plasmas, Vol. 19, 2012, p. 093503.

[12] Mahadevan, S., "Simulation of Direct-Current Surface Plasma Discharges in Air for Supersonic Flow Control," Ph.D. Dissertation, Aero. Eng. and Eng. Mech. Dept., The University of Texas at Austin, Austin, TX, 2010.

[13] Hagelar, G. J. M., and Pitchford, L. C., "Solving the Boltzmann equation to obtain electron transport coefficients and rate coefficients for fluid model," Plasma Sources Science and Technology, Vol. 14, 2005, pp. 722-733.

[14] Houba, T., and Roy, S., "Numerical study of low pressure air plasma in an actuated channel," Journal of Applied Physics, Vol. 118, No. 23, 2015, pp. 1-9.

[15] Rafatov, E. A., Akbar, D., and Bilikmen, S., "Modelling of non-uniform DC driven glow discharge in argon gas," Physics Letters A, Vol. 367, 2007, pp. 114-119.

[16] Deconinck, T., "Simulation Studies of Direct-Current Microdischarges for Electric Propulsion," Ph.D. Dissertation, Aero. Eng. and Eng. Mech. Dept., The University of Texas at Austin, Austin, TX, 2008.

[17] Phelps, A. V., and Petrovic, A. L., "Cold-cathode discharge and breakdown in argon: surface and gas electrons," Plasma Source Science and Technology, Vol. 8, No. 3, 1999, pp. R21-R44.

[18] Deconinck, T., Mahadevan, S., and Raja, L. L., "Computational simulation of coupled nonequilibrium discharge and compressible flow phenomena in a microplasma thruster," *Journal of Applied Physics,* Vol. 106, 2009, p. 063305.

[19] Sitaraman, H., and Raja, L. L., "Simulation studies of RF excited micro-cavity discharge for micro-propulsion applications," Journal of Physics D: Applied Physics, Vol. 45, No. 18, 2012, pp. 1-11.

[20] Boeuf, J. P., Pitchford, L. C., and Schoenbach, K. H., "Predicted properties of microhollow cathode discharges in xenon," Applied Physics Letters, Vol. 86, No. 7, 2005, pp. 1-3.

[21] Scharfetter, D., and Gummel, H., "Large-Signal Analysis of a Silicon Read Diode Oscillator," IEEE Trans. Elec. Dev., Vol. 16, 1969, pp. 64-77.

[22] Goldston, R. J., and Rutherford, P. H., Introduction to Plasma Phyiscs, Intitute of Physics Publishing, Plasma Physics Lab., Princeton University, 1995, p. 150.

[23] Choudhuri, A. R., The Physics of Fluids and Plasmas: an Introduction for Astrophysicists, Cambridge University Press., Cambridge University, Cambridge, United Kingdom, 1998, p. 19.

[24] Raju, R., "Hydrodynamic Model for Investigation of Gas Flows Through Micro-Geometries and Nanopores," M.S. Dissertation, Mech. Eng. Dept., Kettering University, Flint, MI, 2003.

[25] Maurer, J., Tabeling, P., Joseph, P., and Willaime, H., "Second-order slip laws in microchannels for helium and nitrogen," Physics of Fluids, Vol. 15, No. 9, 2003, pp. 2613-2621.

[26] Karniadakis, G. E., Beskok, A., and Aluru, N., Microflows and Nanoflows: Fundamentals and Simulation. Vol. 29, Springer Science-Verlag New York, New York, NY, 2005.

[27] Hanley, H., "The Viscosity and Thermal Conductivity Coefficients of Dilute Argon, Krypton, and Xenon," J. Phys. Chem. Ref. Data, Vol. 2, 1973, pp. 619-642.

[28] Maxwell, J. C., "On Stresses in Rarefied Gases Arising from Inequalities of Temperature," Philosophical Transactions of the Royal Society Part1, Vol. 170, 1879, pp. 231-256.

[29] Agrawal, A., and Prabhu, S. V., "Survey on measurement of tangential momentum accommodation coefficient," Journal of Vacuum Science and Technology A, Vol. 26, No. 4, 2008, pp. 634-645.

[30] Donea, J., and Huerta, A., Finite Element Methods for Flow Problems, John Wiley & Sons, Chichester, England, 2003.

[31] Roy, S., and Pandey, B. P., "Development of a Finite Element-Based Hall-Thruster Model," Journal of Propulsion and Power, Vol. 19, , 2003, pp. 964-971.

[32] Roy, S., Raju, R., Chuang, H., Cruden, B., and Meyyappan, M., "Modeling gas flow through microchannels and nanopores," Journal of Applied Physics, Vol. 93, 2003, pp. 4870-4879).

[33] Roy, S., and Gaintonde, D., "Force interaction of high pressure glow discharge with fluid flow for active separtion control," Physics of Plasmas, Vol. 13, No. 023503, 2006, pp. 1-11.

[34] Kumar, H., and Roy, S., "Multidimensional hydrodynamic plasma-wall model for collisional plasma discharges with and without magnetic field effects," Physics of Plasmas, Vol. 12, No. 093508, 2005, pp. 1-10.

[35] Ketsdever, A. D., Clabough, M. T., Gimelshein, S. F., and Alexeenko, A. A., "Experimental and numerical determination of micropropulsion device efficiencies at low Reynolds number," *AIAA Journal,* Vol. 43, No. 1, 2005, pp. 633-641.

[36] Chen, C. S., Lee, S. M., and Sheu, J. D., "Numerical Analysis of Gas flow in Microchannels," *Numerical Heat Transfer, Part A: Applications,* Vol. 33, 1998, pp. 749-762.

[37] Pong, K. C., Ho, C., Liu, J., and Tai, Y., "Non Linear Pressure Distribution in Uniform Microchannels," *ASME-PUBLICATIONS-FED,* Vol. 197, 1994, p. 51.

[38] Houba, T., "Parallel 3-D Numerical Simulation of Dielectric Barrier Discharge Plasma Actuators," Ph.D. Dissertation, Mech. and Aero. Eng. Dept., University of Florida, Gainesville, FL, 2016.

[39] Godyak, V. A., Piajak, R. B., and Alexandrovich, B. M., "Electrical Characteristics of Parallel-Plate RF Discharges in Argon," *IEEE Transactions on Plasma Science,* Vol. 19, 1991, pp. 660-676.

[40] Pancheshnyi, S., Biagi, S., Bordage, M. C., Hagelaar, G. J. M., Morgan, W. L., and Phelps, A. V., "The LXCat project: Electron scattering cross sections and swarm parameters for low temperature plasma modeling," *Chemical Physics,* Vol. 398, 2012, pp. 148-153.

[41] Finger, G., "Estimtion of Tangential Momentum Accomodation Coefficient Using Molecular Dynamics Simulation," Ph.D. Dissertation, Mech., Mat. and Aero. Eng. Dept., University of Central Florida, Orlando, FL, 2005.

[42] Kang, S. and Oh, H., "On-Orbit Thermal Design and Validation of 1 U Standardized CubeSat of STEP Cube Lab," *International Journal of Aerospace Engineering,* Vol. 2016, 2016, pp. 1-17.

[43] Henninger, J., "Solar Absorptance and Thermal Emittance of Some Common Spacecraft Thermal-Control Coatings," NASA, Washington DC, 1984.